

Near-Infrared Multilayer MoS₂ Photoconductivity-Enabled Ultrasensitive Homogeneous Plasmonic Colorimetric Biosensing

Younggeun Park,* Byunghoon Ryu, Seung Jun Ki, Xiaogan Liang,* and Katsuo Kurabayashi*

The ability to detect low-abundance proteins in human body fluids plays a critical role in proteomic research to achieve a comprehensive understanding of protein functions and early-stage disease diagnosis to reduce mortality rates. Ultrasensitive (sub-fM), rapid, simple “mix-and-read” plasmonic colorimetric biosensing of large-size (≈ 180 kDa) proteins in biofluids using an ultralow-noise multilayer molybdenum disulfide (MoS₂) photoconducting channel is reported here. With its out-of-plane structure optimized to minimize carrier scattering, the multilayer MoS₂ channel operated under near-infrared illumination enables the detection of a subtle plasmonic extinction shift caused by antigen-induced nanoprobe aggregation. The demonstrated biosensing strategy allows quantifying carcinoembryonic antigen in unprocessed whole blood with a dynamic range of 10⁶, a sample-to-answer time of 10 min, and a limit of detection of 0.1–3 pg mL⁻¹, which is ≈ 100 -fold more sensitive than the clinical-standard enzyme-linked immunosorbent assays. The biosensing methodology can be broadly used to realize timely personalized diagnostics and physiological monitoring of diseases in point-of-care settings.

1. Introduction

Nanomaterials manifest unique properties leading to physical phenomena that are not observed in bulk materials. Among such phenomena, localized surface plasmon resonance (LSPR) provides a fundamental basis for biosensor technologies incorporating noble metal nanoparticles.^[1,2] Over the last few

decades, researchers have engaged in an exciting task of applying LSPR-induced optical signal shifts to develop novel and high-performance diagnostic biosensors.^[3–5] The dependence of the optical properties of plasmonic nanoparticles on interparticle separation distances enables colorimetric assays involving the analyte-controlled assembly/aggregation of plasmonic nanoparticles.^[6,7] Nanoparticle assembly-based plasmonic colorimetric assays permit a rapid “one-step” homogeneous assay procedure,^[8] thereby offering a promising alternative to the laborious and time-consuming enzyme-linked immunosorbent assay (ELISA), which has been routinely used as the gold standard in clinical diagnostics. Their simplicity and cost-effectiveness make these assays attractive for point-of-care (POC) testing under limited resources. However, the detection sensitivity and linear dynamic range


of these assays are typically limited due to the inherent weak force of interparticle electrostatic interactions.^[3,4] Additionally, the LSPR shifts in plasmonic colorimetric assays have generally been in the ultraviolet/visible range in which native proteins in physiological fluids (e.g., whole blood (WB)) show high optical absorbance. The optical interferences by cells, platelets, proteins, genes, and biostructures in the sample background can significantly reduce the sensitivity of plasmonic biosensors.^[9–11] This limits the ability to detect directly biomolecules of clinical relevance that are low in abundance at the early onset of progressive disease like cancer.^[12]

To address the issues mentioned above, other “indirect” nanoparticle assembly-based plasmonic colorimetric methodologies have been proposed to improve the sensitivity by amplifying the interaction force during nanoparticle aggregation events. They employ a heterogeneous sandwich immunoassay format with labeling enzyme molecules triggering downstream nanoparticle aggregation by means of catalyzed reactions.^[13,14] In addition, size or morphology changes resulting from analyte-controlled growth or etching of the plasmonic nanoparticles have been demonstrated to amplify the LSPR shifts, enabling ultrasensitive plasmonic colorimetric detection of disease biomarker molecules.^[15] However, involving multiple reagent incubation, washing, enzyme-catalyzed reaction steps, these

Y. Park, B. Ryu, S. J. Ki, X. Liang, K. Kurabayashi
Department of Mechanical Engineering
University of Michigan
Ann Arbor, MI 48109, USA
E-mail: ygpark@umich.edu; xiaoganl@umich.edu; katsuo@umich.edu

Y. Park, X. Liang, K. Kurabayashi
Michigan Center for Integrative Research in Critical Care
University of Michigan
Ann Arbor, MI 48109, USA

K. Kurabayashi
Department of Electrical Engineering and Computer Science
University of Michigan
Ann Arbor, MI 48109, USA

 The ORCID identification number(s) for the author(s) of this article can be found under <https://doi.org/10.1002/admi.202101291>.

DOI: 10.1002/admi.202101291

high-sensitivity methods are more tedious than other formats of ELISA and, perhaps, less convenient for POC testing.^[16,17] Regardless of the assay methodology type, it is necessary to process or dilute a physiological fluid to remove their colored components to ensure “clean” conditions for high-sensitivity plasmonic colorimetric analysis. With many challenges described above, the translation of plasmonic colorimetric biosensor technologies to real-world clinical diagnostics has not been fully fulfilled. This warrants an alternative approach.

Although a number of studies demonstrate naked-eye detection of pathogens and disease markers,^[18,19] a quantitative analysis with high accuracy and high sensitivity still requires high-performance off-chip photodetectors and optical apparatus. Another challenge is the integration of plasmonic biosensors together with optical and fluidic units into a single module. A miniaturized portable module incorporating a sensitive photodetector is imperative for POC testing in various areas, such as clinics, airports, and offices. In recent years, we have demonstrated that an atomically thin layer of molybdenum disulfide (MoS₂) channel integrated into a POC platform enables fast and sensitive colorimetric monitoring of disease-related biomarkers.^[20–22] MoS₂ is a transition metal dichalcogenide material that exhibits superior photo-response characteristics. Specifically, both single- and multi-layer MoS₂ films exhibit an efficient electron-hole pair generation rate under photoexcitation and therefore high photo absorption as compared to silicon, which is the semiconducting material most commonly adopted in modern microelectronics and optoelectronics. Such a high photoresponsivity of MoS₂ is largely attributed to its special 2D band structure which has a high density of van-Hove singularities,^[23] in combination with its 2D surfaces which have much fewer carrier scatters in comparison with those of conventional bulk semiconductors.^[24] The outstanding optoelectronic properties have allowed us to create a high intensity-resolution photodetector with MoS₂ for optoelectronic biosensing applications.^[25–27] However, operated in the ultraviolet/visible range, our previous platforms still require careful sample processing and purification prior to measurement of analyte molecules in complex human physiological fluids.

Here, we report a homogenous plasmonic colorimetric biosensing strategy that allows for highly sensitive wash-free “mix-and-read” quantification of a protein cancer biomarker, carcinoembryonic antigen (CEA), in human biofluids. Our strategy integrates a multilayer MoS₂ photoconductor channel with its properties optimized for near-infrared (NIR) ($\lambda = 650$ nm) operation into an on-chip microfluidic platform. Interestingly, up to the present time, the technological utility of multilayer MoS₂ has been underappreciated in comparison with monolayer MoS₂. Researchers have primarily focused on taking advantage of the capabilities originating from the direct bandgap of monolayer MoS₂ in their studies.^[28] In contrast, we show that multilayer MoS₂ with its layer thickness (≈ 14 nm) is of great value for plasmonic colorimetric biosensing performed under NIR illumination. Such multilayer MoS₂ films exhibit much higher photoresponsivity and light absorption coefficient than monolayer films under NIR illumination, where the background optical interferences of unprocessed physiological fluids are minimized. Furthermore, the relatively thick multilayer MoS₂ channel structure suppresses the carrier scattering effect at the

material interfaces, which buries intrinsic electronic noise in sensor signals and yields an increased signal-to-noise ratio. In our assay, analyte-induced nanoparticle assembly forms plasmonic nanogaps trapping CEA molecules between adjacent particles, which induce plasmonic extinction in the NIR region. Our assay achieves sub-femtomolar detection of CEA in unprocessed WB, urine, and saliva with a dynamic range of 10⁶ and a sample-to-answer time of 10 min.

2. Results and Discussion

In a plasmonic biosensing assay, our integrated on-chip colorimetric reader device enables direct quantification of target proteins in unprocessed WB without any complex optics enabled by the multilayer MoS₂ channel for NIR photodetection (**Figure 1**). The multilayer MoS₂ structure possesses a narrower bandgap than a single-layer or few-layer MoS₂ (FL-MoS₂) structure, which results in highly efficient photoexcitation of free electron carriers under NIR illumination. After a biofluid (e.g., WB, urine, and saliva) sample is mixed with antibody-modified gold nanoparticles (AuNPs) and directly loaded onto a 2.5 μ L-volume micro-chamber of the device, analyte-induced AuNP aggregation leads to the formation of antibody-protein-nanoparticle complex (plasmo-biomarker composite) (**Figure 1a**). Molecules, cells, and tissues in complex biological systems exhibit a weaker absorption for NIR radiation than that for visible radiations.^[29,30] Therefore, the NIR operation of the biosensor brings the minimized influence of the background absorbance to the measurement (**Figure 1b**). Our assay achieves sample preparation-free, wash-free colorimetric biosensing of target proteins by measuring the NIR absorbance shift upon the plasmo-biomarker composite formation with the multilayer MoS₂ photodetector underneath the micro-chamber.

2.1. NIR Photoconductivity of Multilayer MoS₂ Structure

To achieve the NIR ultra-fine sensing resolution in the assay, we focused on understanding the properties of a multilayer MoS₂ channel (**Figure 2**). The MoS₂ channel has a smooth surface and a structure formed by the stack of multiple pristine monolayers. These structural characteristics are expected to yield minimal charge trapping and scattering of photo-generated carriers, therefore leading to large NIR light absorption (**Figure 2a**). We fabricated the MoS₂ channel by a micro-printing method for the purpose of controlling its surface properties and the number of the stacked monolayers (see “Experimental Section” and **Figure S1**, Supporting Information).^[31] The multilayer MoS₂ structure has an effective channel length of ≈ 1 μ m laterally sandwiched by a pair of Ti/Au pads, which secures a single-crystal, single-domain structure because the mean size of crystal domains is in the order of 100 s μ m–1 s mm. The optimized MoS₂ channel has a nominal thickness of 14.5 nm with $\pm 5\%$ tolerance along the path, as determined by atomic force microscopy (AFM) (**Figure 2b** and **Figures S2** and **S3**, Supporting Information). The excellent photoresponsivity of the channel under NIR was reflected by significantly enhanced photocurrent, I_{ph} , that was more than 100 times larger than

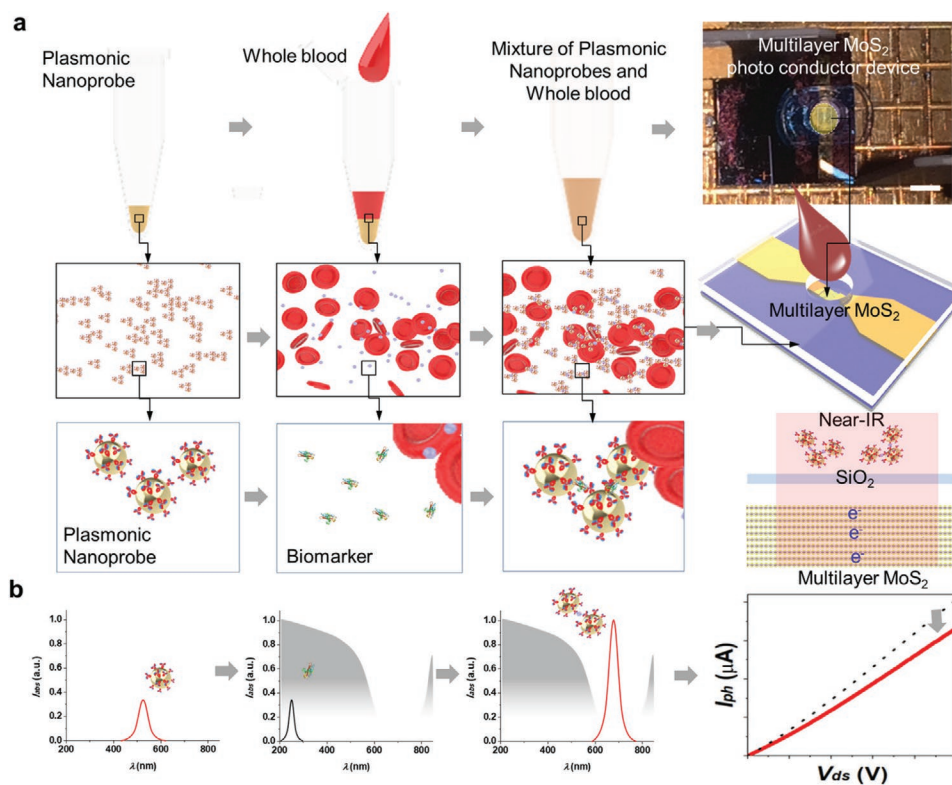


Figure 1. Concept of multilayer MoS₂ photoconductivity-enabled NIR “mix-and-read” plasmonic colorimetric assay for cancer biomarker detection. a) Mixing of a colloidal solution suspending antibody-conjugated plasmonic nanoparticles and WB. The mixture is loaded onto an on-chip colorimetric reader (photo conductor device) operated in the NIR region. The device consists of a SiO₂/polydimethylsiloxane (PDMS) micro-chamber layer and a multilayer MoS₂ photoconducting channel on a silicon substrate. The presence of target cancer biomarker in WB induces the aggregation/assembly of antibody-conjugated nanoparticles (i.e., nanoprobes). Multilayer-MoS₂ exhibits high photoresponsivity to NIR excitation illumination. b) Extinction spectrum of a solution suspending dispersed plasmonic nanoprobes (left), blood constituents (center), and aggregated/assembled plasmonic nanoprobes (right). An extinction peak shift occurs due to the plasmonic coupling effect caused by biomarker-controlled nanoparticle aggregation. The shift is detected as a decrease in the photocurrent signal of the multilayer MoS₂ photoconducting channel under NIR illumination. The background absorbance of WB is small in the NIR region.

the dark current at a source-drain voltage, V_{ds} , of 1 V at $\lambda = 650$ nm and $P = 2.4$ mW (Figure 2c). The photoresponsivity of this MoS₂ channel reached a lower bound at $\lambda = \approx 750$ nm. This wavelength corresponds to a photon energy of ≈ 1.653 eV that matches the bandgap of the previously reported multilayer MoS₂.^[27,32] The photocurrent value was found to increase almost linearly with increasing the incident light power, P (Figure S4, Supporting Information). Under the same light illuminating condition, the light on/off cycle test shows consistent and rapid device response characteristics (Figure 2d). As a function of the MoS₂ channel thickness, the measured photocurrent reveals the highest for 14 nm thick channel (Figure 2e). Especially, this 14 nm thick MoS₂ channel exhibited threefold higher photoresponsivity than the monolayer channel within the NIR region (Figure 2f). Furthermore, the noise equivalent power (NEP) density of the multilayer MoS₂ channel (14 nm thick channel) was over 1000 times smaller than that of a high-profile cadmium sulfide (CdS) photodetector, and it approached the noise floor of the external electronic analysis system at the frequency > 10 Hz (Figure 2g).

The low electronic-noise level above can be attributed to the combination of several critical material features, including 1) single-crystallinity of the multilayer MoS₂ channel (free of

crystal domain boundaries), 2) atomic-scale smoothness of the 2D channel surface with an extremely low density of dangling bonds and defects, and 3) the larger thickness (10–20 nm) that can minimize the substrate scattering effect.^[29,30] These material features are beneficial to yield much fewer surface scattering centers for photoexcited carriers and, therefore, the photo-response of devices made from multilayer MoS₂ is expected to yield a much lower internal electronic noise level in comparison with those made from conventional bulk semiconductors.^[23,24,33] To support these arguments, we further compared the RMS noise values measured from a 14-nm thick pristine multilayer MoS₂ channel (the same one used in the biosensor), a 3 nm-thick pristine few-layer MoS₂ channel, whose transport properties are expected to be more sensitive to substrate scattering as compared to multilayer MoS₂, and a 14 nm-thick multilayer MoS₂ channel treated with O₂ plasma, which is expected to have more surface defects and scattering centers for photoexcited carriers (Figure 2h). This comparison shows that the 14-nm thick pristine multilayer channel exhibits the lowest RMS noise level, nearly 100-fold smaller than those measured from the other two channels. This comparison results support aforementioned explanations for the low internal electronic noise level achieved in pristine multilayer MoS₂ photo-response channels.

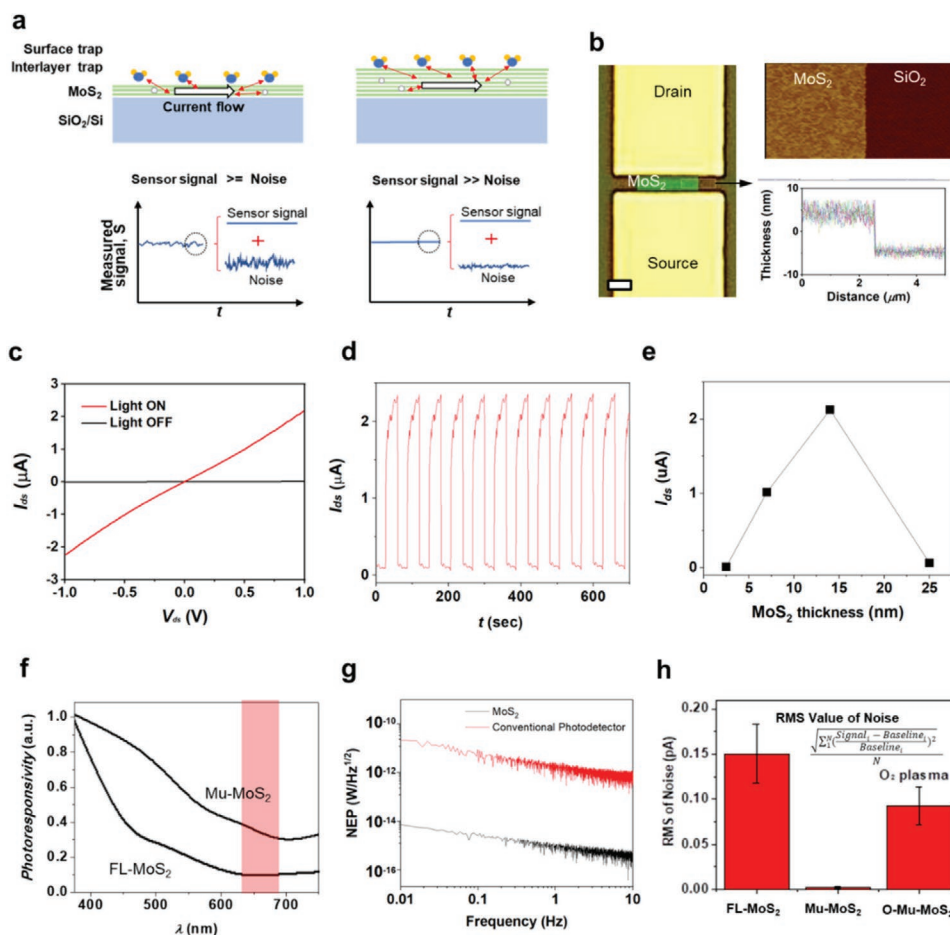


Figure 2. Multilayer MoS₂ photoconducting channel with ultra-low internal electronic noise. a) Illustration of photoexcited carrier transport in a multilayer MoS₂ channel; b) Optical micrograph and AFM images showing the profile of a 14 nm-thick, 1 μm-long multilayer MoS₂ channel with electrodes; c) Drain-source current (I_{ds})- drain-source voltage (V_{ds}) characteristics of the multilayer MoS₂ channel under a dark condition and under light illumination at $\lambda = 650$ nm and $P \approx 2.4$ mW; I_{ds} linearly increases from 0.03 to 2.1 μA with V_{ds} varied from 0 to 1.0 V, whereas, the dark current changes from 0.002 to 0.051 μA with the same V_{ds} range; d) Photocurrent enhancement with a consistent cycle under alternating ON and OFF modes of illumination under light illumination at $\lambda = 650$ nm and $P \approx 2.4$ mW; e) I_{ds} as a function of the MoS₂ layer thickness under light illumination at $\lambda = 650$ nm and $P \approx 2.4$ mW; f) Photoresponsivity spectrum of multilayer MoS₂ and monolayer MoS₂. The photoresponsivity is given as $R = I_{ph}/P_{in}$, where I_{ph} is the photocurrent and P_{in} is the power density of the incident light; g) NEP density of the multilayer MoS₂ and a commercial CdS photodetector; h) RMS noise values measured for two smooth-surface pristine MoS₂ channels of 3 and 14 nm in thickness, respectively, and for an O₂ plasma-treated 14 nm-thick MoS₂ channel with a rough surface.

2.2. NIR Nanoparticle Aggregation-Based Plasmonic Colorimetric Biosensing

With the NIR photoconduction capability and ultra-low noise level of the multilayer MoS₂ channel, we designed an on-chip colorimetric reader device and demonstrated NIR plasmonic colorimetric biosensing (Figure 3). The device integrates an optically transparent SiO₂/polydimethylsiloxane (PDMS) micro-chamber layer and the multilayer MoS₂ photoconducting channel on a silicon chip (Figure S5, Supporting Information). According to the geometry of the multilayer MoS₂ channel shown in Figure 2, the micro-chamber layer was designed and assembled using photo lithographically patterned alignment marks (see “Experimental Section” and “Supporting Information”). To validate our ultrasensitive biomolecular detection capability, we employed CEA as the target analyte. Clinical blood testing measures CEA as one of the important cancer

biomarkers,^[34] and CEA has been also approved for assessing tumor burden in patients already diagnosed with cancer, particularly during therapy of advanced cancer.^[35–38] Sensitive assessment of CEA together with other blood protein markers is essential for early cancer screening.^[39]

Antigen-antibody binding events induce the assembly of antibody-conjugated AuNP probes in a sample solution (Figure 3a). The assembled AuNPs result in plasmonic coupling over the interparticle nanogap and causes the change of transmission light intensity through the AuNP-suspended solution. Achieving high detection sensitivity requires the interparticle spacing of AuNP probes to be smaller than the nanoparticle diameter. The appropriate spacing assures a distinct optical transition of assembled nanoparticles.^[40] Considering the sizes of the antibody and protein molecules of CEA, we used anti-CEA antibody-modified AuNP (anti-CEA/AuNP) probes of 50 nm in diameter for our assay. A scanning electron microscopy

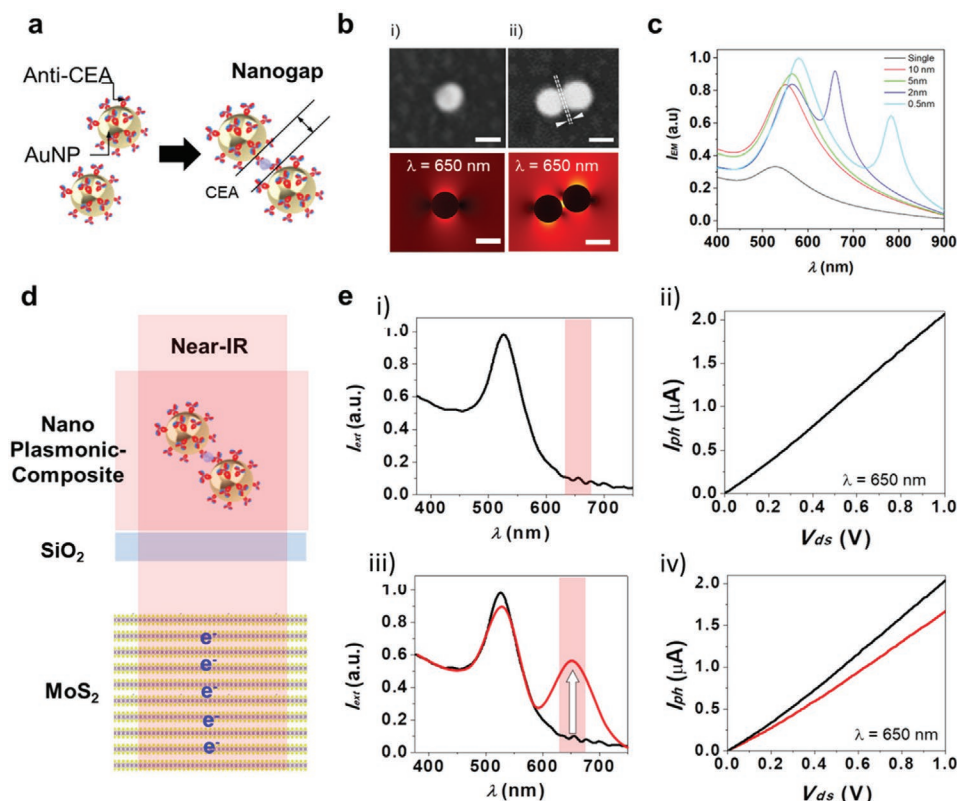


Figure 3. Performance of AuNP aggregation-based plasmonic colorimetric assay using multilayer MoS₂ photoconductivity. a) Schematic of plasmonic nanogap resulting from interactions between anti-CEA/AuNP probes and CEA protein; b) SEM images (top) and FEA simulations of near-field *E*-field distributions at $\lambda = 650$ nm (bottom) of i) a single anti-CEA/AuNP probe dispersed in the absence of CEA in a PBS solution and ii) a pair of anti-CEA/AuNP probes assembled in the presence of CEA in the same solution (Scale bar: 50 nm). c) Extinction spectrum of anti-CEA/AuNP probe-suspending PBS as a function of the nanogap distance; d) Integration of NIR nanoprobe-aggregation plasmonic colorimetric biosensing and multilayer MoS₂ photodetection on a single module; e) i) Extinction spectrum and ii) photocurrent measured for a PBS solution suspending anti-CEA/AuNP probes with no CEA. iii) Extinction spectrum and iv) photocurrent measured for a PBS solution suspending aggregated anti-CEA/AuNP probes with CEA at $C_{\text{CEA}} = 10^1$ ng mL⁻¹.

(SEM) image allowed us to confirm that the anti-CEA/AuNP probes assembled in the presence of CEA formed a nanoscale interparticle gap < 3 nm (Figure 3b). Our finite element analysis (FEA) simulation of the local electric (*E*) field indicates strong plasmonic coupling at $\lambda = 650$ nm in the near-field of the nanoscale gaps between the assembled anti-CEA/AuNP probes with the size selected above (see “Experimental Section”) (Figure 3c).

Our biosensing strategy performs colorimetric detection of analyte-controlled assembly/aggregation of anti-CEA/AuNP probes in a sample solution by the NIR-operated multilayer MoS₂ photoconducting channel (Figure 3d). Under light illumination ($\lambda = 650$ nm), the absence of CEA allows the incident light to penetrate through the solution in the micro-chamber layer with the highest transmission, and the incident light is maximally delivered to the underlying MoS₂ channel (Figure 3e). On the contrary, the presence of CEA in the solution leads to the analyte-induced assembly of anti-CEA/AuNP probes. This results in plasmonic coupling that increases the absorbance of the solution around $\lambda = 650$ nm. The absorbance varies with the CEA concentration (C_{CEA}). Thus, C_{CEA} is determined by the photocurrent signal of the MoS₂ channel.

2.3. Integrated NIR Plasmonic Colorimetric MoS₂ Assay

In the basis of the aforementioned detection principle, we performed NIR plasmonic colorimetric MoS₂ assay (Figure 4). Firstly, using a photospectrometer (Synergy Neo2, BioTek), we measured the extinction spectrum of anti-CEA/AuNP probe-suspending phosphate-buffered saline (PBS) solution that is spiked with CEA of various concentrations (Figure 4a). The extinction spectrum had a local absorbance peak around $\lambda = \approx 650$ nm, and we observed that the absorbance increased with the CEA concentration. However, we were unable to detect subtle absorbance peak changes at the concentration below 10^{-1} ng mL⁻¹ using the commercial instrument. Now, we used the multilayer MoS₂ channel photodetector to analyze the AuNP aggregation-induced NIR optical extinction in the assay (see “Experimental Section”). We quantified dynamic photocurrent, I_{ph} obtained at a given CEA concentration relative to the signal from the blank (no CEA) sample, $I_{\text{ph}0}$, and normalized its values at various CEA concentrations as photocurrent variations, $\Delta I_{\text{ph}}/I_{\text{ph}0} = (I_{\text{ph}} - I_{\text{ph}0})/I_{\text{ph}0}$ (Figure 4b). The optical extinction induced by anti-CEA/AuNP probe aggregation reduced the photocurrent of the MoS₂ channel with the increasing CEA concentration. The dynamic curves of $\Delta I_{\text{ph}}/I_{\text{ph}0}$ show plateaus within 10 min

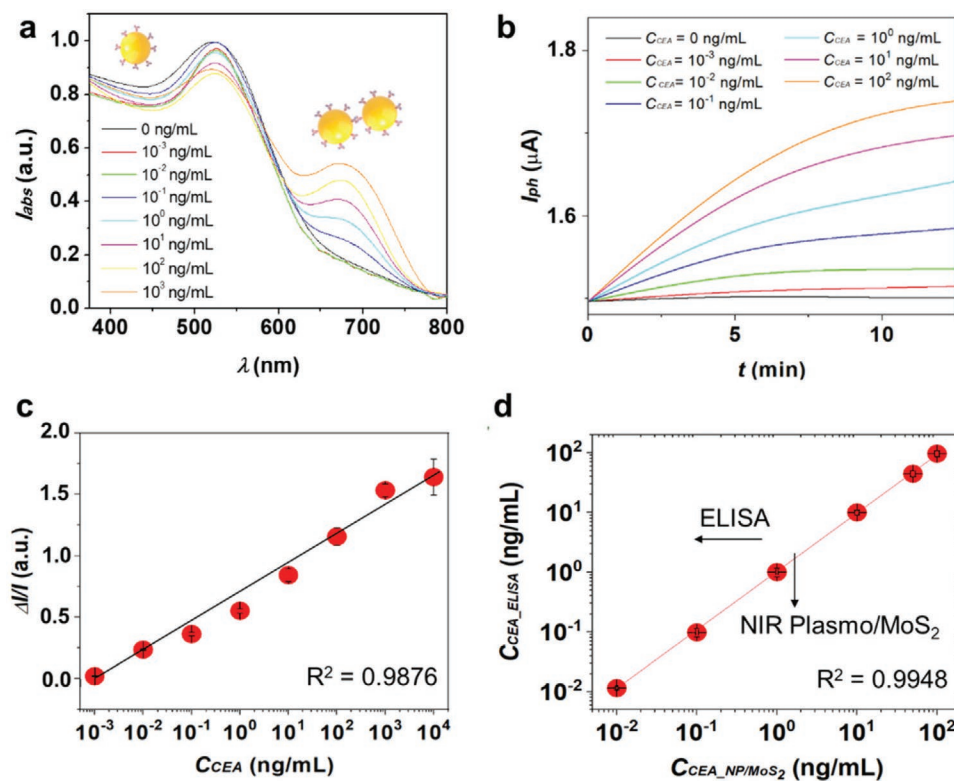


Figure 4. Performance of AuNP aggregation-based plasmonic colorimetric assay using multilayer MoS₂ photoconductivity a) Extinction spectrum of anti-CEA/AuNP probe-suspending PBS as a function of the CEA concentration, C_{CEA} , from 10^{-3} to 10^3 ng mL⁻¹, which is obtained by a photospectrometer (Synergy Neo2, BioTek); b) Time evolution of the normalized relative photocurrent $\Delta I_{ph}/I_{ph0}$ signal for various levels of C_{CEA} , where I_{ph0} is the photocurrent value at $C_{CEA} = 0$. Each signal curve is measured during an assay incubation process where anti-CEA/AuNP probe aggregation progresses over time; c) Constructed calibration curve based on $\Delta I_{ph}/I_{ph0}$ as a function of C_{CEA} ($n = 5$); d) Linear regression between the NIR plasmonic colorimetric (NIR PlasmO/MoS₂) assay and ELISA data for the same samples spiked with CEA at C_{CEA} ranging from 10^{-2} to 10^2 ng mL⁻¹ ($n = 5$).

for all CEA concentrations, which represents the endpoint of the assay. The obtained I_{ph} could distinguish the signal at the low CEA concentration from the basal signal. This proves that the multilayer MoS₂ photoconductivity-enabled NIR plasmonic colorimetry permits high-sensitivity biomarker detection.

From the data above, we further obtained a standard curve of the assay for CEA in PBS (Figure 4c). It reveals a linear dynamic range of detection from 10^{-3} to 10^3 ng mL⁻¹ with the limit of detection (LOD) estimated to be as low as 0.11×10^{-3} ng mL⁻¹ (see “Experimental Section”). The linear dynamic range and LOD of our colorimetric biosensor assay are 100-fold greater and ≈ 200 -fold lower than those of the standard ELISA, respectively (dynamic range: 10^{-1} – 10^3 ng mL⁻¹, LOD: $\approx 2 \times 10^{-1}$ ng mL⁻¹) (Table S1, Supporting Information).^[41,42] The assay data showed a linear ($R^2 = 0.9948$) correlation with ELISA measurement of the same samples at the CEA concentration between 10^0 and 10^3 ng mL⁻¹ (Figure 4d). These results indicate that the plasmonic colorimetric MoS₂ assay enables ultrasensitive, rapid, simple, mix-and-read, and ultralow-noise detection of CEA levels.

2.4. Wash-Free Homogeneous Detection of Body-Fluid Cancer Biomarker

Subsequently, we demonstrated wash-free homogeneous detection of CEA in human WB, urine, and saliva (Figure 5). The

extinction spectra of these biofluids show significantly lower NIR absorbance than that of PBS suspending aggregated anti-CEA/AuNP probes with 10^0 ng mL⁻¹ of CEA (Figure 5a). To run a control experiment, we measured the photocurrent of the device at two different illumination wavelengths of $\lambda = 532$ and 650 nm for non-spiked WB, urine, saliva, and PBS. The larger value of I_{ph0} at $\lambda = 650$ nm reflects the smaller background interferences of the biofluids in the NIR region (Figure 5b). We obtained standard calibration curves for CEA in WB with these two illumination wavelengths (Figure 5c and Figure S6, Supporting Information). The curve at $\lambda = 650$ nm has a distinctly linear shape with a 6-log detection range and a LOD of 3.5×10^{-3} ng mL⁻¹, which ensures a high-performance assay. Meanwhile, interrupted by the background absorption, we found no noticeable sensor signal variations with the concentration in the curve at $\lambda = 532$ nm. Thus, the control experiment proves the remarkable advantage of the NIR-operated colorimetric biosensing strategy. The data from the NIR assay using unprocessed WB yielded a good linear correlation with the data for PBS ($R^2 = 0.9914$) (Figure 5d and Figure S7, Supporting Information). We additionally validated the specificity of the assay to the target analyte by using WB spiked with a mixture of CEA and cancer antigen (CA)-19 (Figure 5e). The data prove the negligible cross-reactivity of the anti-CEA/AuNP probes with the other proteins.

Quantitative detection of CEA in urine and saliva is of great importance in the context of realizing a simple, convenient

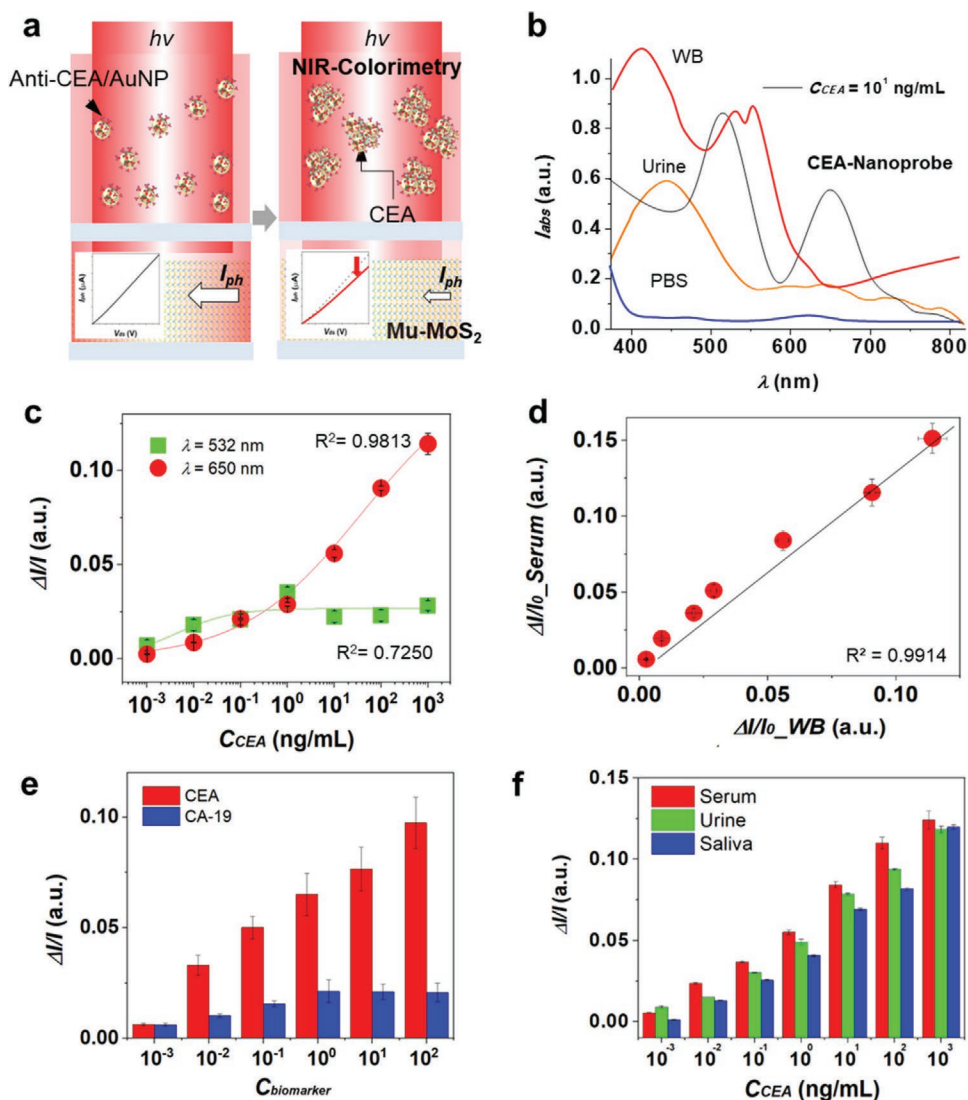


Figure 5. Detection performance in various mediums. a) Schematic of human WB CEA detection; b) Extinction spectra of WB, urine, PBS, and PBS suspending aggregated anti-CEA/AuNP probes with 10^1 ng mL^{-1} of CEA; c) Measured I_{ph} variation ($\Delta I_{ph}/I_{ph0}$) as a function of C_{CEA} from 10^{-3} to 10^3 ng mL^{-1} in WBA at $\lambda = 532$ and 650 nm with 2.5 mW cm^{-2} ($n = 5$); d) Linear regression between data from human serum and human WB CEA detections. The data are obtained for samples from the same donor. Both samples are spiked with CEA at C_{CEA} , ranging from 10^{-2} to 10^2 ng mL^{-1} ($n = 5$); e) Bar graph showing the normalized photocurrent signal changes resulting from the anti-CEA/AuNP probe-based assay testing a mixture of two key cancer biomarkers: CEA (ng mL^{-1}) and CA-19 (U mL^{-1}) in WB. The height of each bar represents the percent change in the scattered light intensity after 10 min of the exposure of the anti-CEA/AuNP probes to the mixture sample. Error bars correspond to standard errors across 10 samples; f) Calibration standard curves showing the normalized photocurrent shift, $\Delta I_{ph}/I_{ph0}$, at C_{CEA} ranging from 10^{-3} to 10^3 ng mL^{-1} in serum, urine, and saliva at $\lambda = 532 \text{ nm}$ and 650 nm with $P = 2.5 \text{ mW cm}^{-2}$ ($n = 5$).

non-invasive cancer screening test. However, CEA is known to be a low-abundance biomarker in these fluids ($\approx 0.2 \text{ ng mL}^{-1}$ and $\approx 1 \text{ ng mL}^{-1}$ in urine and saliva, respectively).^[9,10,43,44] We additionally tested our ability to quantify CEA in these biofluids without sample processing and observed similar results to that of a serum test (Figure 5f). For the saliva solution, the biosensor signal, $\Delta I_{ph}/I_{ph0}$, linearly ($R^2 = 0.9453$) increased with the CEA concentration ranging from 10^{-3} to 10^3 ng mL^{-1} , and the LOD was determined to be $0.92 \times 10^{-3} \text{ ng mL}^{-1}$. The data for the urine solution fitted a slightly less linear curve ($R^2 = 0.9712$), and the LOD was estimated to be $0.57 \times 10^{-3} \text{ ng mL}^{-1}$. These LOD values validate that the assay can detect CEA even at

≈ 1000 -fold lower concentrations than the clinical baseline. We believe that rapid and sensitive non-invasive immunodiagnosics is highly feasible with our homogenous assay strategy when applied for the detection of clinically validated saliva/urine biomarkers.

3. Conclusion

So far, we have demonstrated ultrasensitive plasmonic colorimetric biosensing of biofluid proteins by using a micro-printed MoS_2 channel as an integrated photodetector, which

forms a stack of multiple semiconducting atomic monolayers. The material structure of the MoS₂ channel with an atomically smooth surface, a single domain, and a buffer from the substrate promise to allow NIR radiation-excited carriers to efficiently transport under a source-drain bias by suppressing scattering events at the surface, grain boundary, and substrate. The low-carrier scattering property is reflected by the 100-fold smaller electronic noise as compared to those obtained for the thin monolayer and O₂ plasma-treated multilayer MoS₂ channels. Importantly, the ultralow-noise multilayer MoS₂ channel photodetection played a pivotal role in detecting subtle optical transitions caused by analyte-induced AuNP aggregation. The NIR operation of the multilayer MoS₂ channel-based colorimetric reader serves to significantly reduce the background absorbance of the biofluid, which makes it possible to detect the analyte signal, not masked by background interferences. As a result, our method can achieve the wash-free, mix-and-detection immunoassay of CEA in clinically relevant biofluids, such as WB, urine, saliva, and serum.

Previous nanoparticle aggregation-based colorimetric assays permitting direct analyte quantification still require nanoparticle surface modification with small-sized synthetic affinity elements (e.g., aptamers and peptides)^[45–48] or nanoparticle cross-linking^[49] to fill the gap caused by the weak plasmon coupling effect. In contrast, our biosensing strategy achieves the ultrasensitive performance even if using widely common chemistry for the antibody modification of AuNPs, which makes it easy to adapt the method to various assays using a wide variety of antigen-antibody combination types. It follows that this strategy can be broadly employed in biomarker-guided early diagnosis and personalized monitoring of both acute and chronic diseases. Furthermore, the plasmonic colorimetric assay could achieve higher throughput by incorporating an array-type device similar to the one demonstrated in our other study.^[21] The proposed rapid, sensitive, selective, user-friendly on-chip biosensing technology may provide a promising platform for POC testing in a clinical setting outside a regular hospital or a clinic lab. It may also find wide use in future blood biomarker-guided cancer diagnostics, potentially eliminating cost, time, inconvenience, and invasiveness imposed by conventional cancer screening techniques, such as mammography, colonoscopy, tissue biopsy, radiological imaging, and genetic testing.

4. Experimental Section

Multilayer MoS₂ Fabrication: The authors employed a micro-printing method to fabricate a multilayer MoS₂ photoconducting channel on a silicon substrate coated with a thermally grown SiO₂ film (see “Supporting information”). The printed MoS₂ channel had a thickness of ≈14.5 nm and sufficient photoresponsivity at $\lambda = \approx 650$ nm. The topography of the MoS₂ channel was characterized by using an AFM (Bruker ICON AFM). The obtained topographical data were post-processed using commercial software (Nanoscope Analysis). The fabrication of these MoS₂ channels followed the same lithographical patterning/etching methods as in Figure S2, Supporting Information.

Characterization of Multilayer MoS₂: Topography, photo enhancement, photoresponsivity, and noise properties of the fabricated multilayer MoS₂ channel were characterized using an AFM (Bruker ICON AFM), a conventional power/ wavelength meter (OMM-6810B-100V, Newport),

a semiconductor analyzer (HP-4145B), and a noise parameter analyzer (Keithley 4200s). To benchmark the photodetection performance of the multilayer MoS₂ channel, the noise power spectral density (i_N^2/Hz) of a commercial CdS photodetector was also measured (see “Supporting information”).

NIR Plasmonic Nanoprobe: For the NIR plasmonic colorimetric assay, plasmonic probes were designed and synthesized that consistently aggregate upon their selective binding to CEA (see Supporting Information). First, a gold nanoparticle colloidal solution was prepared.^[50] Then, the established surface chemistry protocols^[51,52] were applied to form a self-assembled monolayer of antibodies on each AuNP surface. To suppress non-specific binding on the nanoparticle surfaces, the prepared anti-CEA/AuNP probes were treated with a blocking buffer of 1% BSA in 1 × PBS and incubated them for 20 min. After the anti-fouling process, the structural uniformity and dispersion of the probes were confirmed using a UV–VIS spectrometer (Agilent 8453 G1103A Spectrophotometer).

Colorimetric Reader Device Fabrication: To construct the reader device used for the plasmonic colorimetric assay, a PDMS micro-chamber layer was first fabricated with its bottom sealed by a thin (250 μm) cover glass substrate separately from the silicon substrate holding the multilayer MoS₂ channel above. Using lithographically patterned alignment marks, the features on the micro-chamber layer were manually aligned to the multilayer MoS₂ channel pattern on the silicon substrate. Then, to assemble the whole device, the cover glass side of the micro-chamber layer was attached onto the top of the electrode patterns on the silicon substrate with a surgical adhesive. All measurements of the reader device were performed using an optoelectronic setup. The setup includes an overhead laser (power density, 2.5 mW/cm^2), a probe station (Lakeshore), a semiconductor parameter analyzer (HP-4145B) and a conventional power and wavelength meter (OMM-6810B-100V, Newport). The plasmonic colorimetric assay was validated by comparing its data with ELISA test results (see “Supporting information”).

Electromagnetic Field Simulation: The authors conducted an FEA (COMSOL Multiphysics software) and predicted near-field electromagnetic fields around a disperse AuNP and assembled AuNPs by solving Helmholtz wave equation (see “Supporting information”).

Sampling and Handling Biofluid Samples: Human blood samples were drawn from healthy donors after obtaining informed consent according to an Institutional Review Board (IRB)-approved protocol (protocol HUM00115179/UMCC 2016.051). Artificial saliva and urine were used, prepared by the established standard protocols (see details in “Supporting information”). Using these biofluids, standard samples spiked with known concentrations of CEA were prepared.

Supporting Information

Supporting Information is available from the Wiley Online Library or from the author.

Acknowledgements

Y.P. and B.R. contributed equally to this work. This work was supported by the National Science Foundation, NSF-ECCS program (1708706), NSF-CBET program (2030551), and academic research fund and Mcubed (U064088) at the University of Michigan. The fabrication of MoS₂ devices was partially supported by NSF-CMMI program (2001036).

Conflict of Interest

The authors declare no conflict of interest.

Data Availability Statement

The data that support the findings of this study are available from the corresponding author upon reasonable request.

Keywords

carcinoembryonic antigen detection, localized surface plasmon resonance, multilayer MoS₂, plasmonic colorimetric biosensors, point-of-care immunoassay

Received: July 21, 2021

Revised: October 1, 2021

Published online: November 17, 2021

- [1] K. Saha, S. S. Agasti, C. Kim, X. Li, V. M. Rotello, *Chem. Rev.* **2012**, *112*, 2739.
- [2] K. A. Willets, R. P. V. Duyne, *Annu. Rev. Phys. Chem.* **2007**, *58*, 267.
- [3] P. D. Howes, S. Rana, M. M. Stevens, *Chem. Soc. Rev.* **2014**, *43*, 3835.
- [4] L. Tang, J. Li, *ACS Sens.* **2017**, *2*, 857.
- [5] W. Zhou, X. Gao, D. Liu, X. Chen, *Chem. Rev.* **2015**, *115*, 10575.
- [6] Z. Gao, Z. Qiu, M. Lu, J. Shu, D. Tang, *Biosens. Bioelectron.* **2017**, *89*, 1006.
- [7] Z. Gao, M. Xu, L. Hou, G. Chen, D. Tang, *Anal. Chem.* **2013**, *85*, 6945.
- [8] D. A. Giljohann, D. S. Seferos, W. L. Daniel, M. D. Massich, P. C. Patel, C. A. Mirkin, *Angew. Chem., Int. Ed.* **2010**, *49*, 3280.
- [9] R. S. Gaster, D. A. Hall, C. H. Nielsen, S. J. Osterfeld, H. Yu, K. E. Mach, R. J. Wilson, B. Murmann, J. C. Liao, S. S. Gambhir, S. X. Wang, *Nat. Med.* **2009**, *15*, 1327.
- [10] R. M. Nagler, *Oral Oncol.* **2009**, *45*, 1006.
- [11] D. Sidransky, *Nat. Rev. Cancer* **2002**, *2*, 210.
- [12] L. Wu, X. Qu, *Chem. Soc. Rev.* **2015**, *44*, 2963.
- [13] Y. Xianyu, Y. Chen, X. Jiang, *Anal. Chem.* **2015**, *87*, 10688.
- [14] X.-M. Nie, R. Huang, C.-X. Dong, L.-J. Tang, R. Gui, J.-H. Jiang, *Biosens. Bioelectron.* **2014**, *58*, 314.
- [15] L. Rodríguez-Lorenzo, R. de la Rica, R. A. Álvarez-Puebla, L. M. Liz-Marzán, M. M. Stevens, *Nat. Mater.* **2012**, *11*, 604.
- [16] R. Ren, G. Cai, Z. Yu, D. Tang, *Sens. Actuators, B* **2018**, *265*, 174.
- [17] R. Ren, G. Cai, Z. Yu, Y. Zeng, D. Tang, *Anal. Chem.* **2018**, *90*, 11099.
- [18] P. Moitra, M. Alafeef, K. Dighe, M. B. Frieman, D. Pan, *ACS Nano* **2020**, *14*, 7617.
- [19] R. de la Rica, R. M. Stevens, *Nat. Nanotechnol.* **2012**, *7*, 821.
- [20] Y. Park, B. Ryu, Q. Deng, B. Pan, Y. Song, Y. Tian, H. B. Alam, Y. Li, X. Liang, K. Kurabayashi, *Small* **2020**, *16*, 1905611.
- [21] Y. Park, B. Ryu, S. J. Ki, B. McCracken, A. Pennington, K. R. Ward, X. Liang, K. Kurabayashi, *ACS Nano* **2021**, *15*, 7722.
- [22] Y. Park, B. Ryu, B.-R. Oh, Y. Song, X. Liang, K. Kurabayashi, *ACS Nano* **2017**, *11*, 5697.
- [23] L. Britnell, R. M. Ribeiro, A. Eckmann, R. Jalil, B. D. Belle, A. Mishchenko, Y.-J. Kim, R. V. Gorbachev, T. Georgiou, S. V. Morozov, A. N. Grigorenko, A. K. Geim, C. Casiraghi, A. H. C. Neto, K. S. Novoselov, *Science* **2013**, *340*, 1311.
- [24] S. Wi, M. Chen, H. Nam, A. C. Liu, E. Meyhofer, X. Liang, *Appl. Phys. Lett.* **2014**, *104*, 232103.
- [25] A. Splendiani, L. Sun, Y. Zhang, T. Li, J. Kim, C.-Y. Chim, G. Galli, F. Wang, *Nano Lett.* **2010**, *10*, 1271.
- [26] S. Lebégue, O. Eriksson, *Phys. Rev. B* **2009**, *79*, 115409.
- [27] K. F. Mak, C. Lee, J. Hone, J. Shan, T. F. Heinz, *Phys. Rev. Lett.* **2010**, *105*, 136805.
- [28] K. F. Mak, J. Shan, *Nat. Photonics* **2016**, *10*, 216.
- [29] E. J. Vankampen, W. G. Zijlstra, *Adv. Clin. Chem.* **1983**, *23*, 199.
- [30] C.-L. Tsai, J.-C. Chen, W.-J. Wang, *Journal of Medical and Biological Engineering* **2001**, *21*, 7.
- [31] M. Chen, H. Nam, H. Rokni, S. Wi, J. S. Yoon, P. Chen, K. Kurabayashi, W. Lu, X. Liang, *ACS Nano* **2015**, *9*, 8773.
- [32] Y. Zhihao, O. Zhun-Yong, L. Songlin, X. Jian-Bin, Z. Gang, Z. Yong-Wei, S. Yi, W. Xinran, *Adv. Funct. Mater.* **2017**, *27*, 1604093.
- [33] S. Wi, H. Kim, M. Chen, H. Nam, L. J. Guo, E. Meyhofer, X. Liang, *ACS Nano* **2014**, *8*, 5270.
- [34] A. K. Mattox, C. Bettgowda, S. Zhou, N. Papadopoulos, K. W. Kinzler, B. Vogelstein, *Sci. Transl. Med.* **2019**, *11*, eaay1984.
- [35] S. Hammarström, *Semin. Cancer Biol.* **1999**, *9*, 67.
- [36] L. Hernández, A. Espasa, C. Fernández, A. Candela, C. Martín, S. Romero, *Lung Cancer* **2002**, *36*, 83.
- [37] F. Naghibalhossaini, P. Ebadi, *Cancer Lett.* **2006**, *234*, 158.
- [38] S. P. Prete, L. Rossi, P. P. Correale, M. Turriziani, S. Baier, G. Tamburrelli, L. De Vecchis, E. Bonmassar, A. Aquino, *Pharmacol. Res.* **2005**, *52*, 167.
- [39] J. D. Cohen, L. Li, Y. Wang, C. Thoburn, B. Afsari, L. Danilova, C. Douville, A. A. Javed, F. Wong, A. Mattox, R. H. Hruban, C. L. Wolfgang, M. G. Goggins, M. Dal Molin, T.-L. Wang, R. Roden, A. P. Klein, J. Ptak, L. Dobbyn, J. Schaefer, N. Silliman, M. Popoli, J. T. Vogelstein, J. D. Browne, R. E. Schoen, R. E. Brand, J. Tie, P. Gibbs, H.-L. Wong, A. S. Mansfield, J. Jen, S. M. Hanash, M. Falconi, P. J. Allen, S. Zhou, C. Bettgowda, L. A. Diaz, C. Tomasetti, K. W. Kinzler, B. Vogelstein, A. M. Lennon, N. Papadopoulos, *Science* **2018**, *359*, 926.
- [40] D. Aili, M. M. Stevens, *Chem. Soc. Rev.* **2010**, *39*, 3358.
- [41] P. L. Wei, L. T. Lee, L. M. Tseng, K. W. Huang, *Sci. Rep.* **2018**, *8*, 10002.
- [42] X. Yuan, T. Bian, J. Liu, H. Ke, J. Feng, Q. Zhang, L. Qian, X. Li, Y. Liu, J. Zhang, *Oncotarget* **2017**, *8*, 59324.
- [43] G. M. Saied, W. H. El-Metenawy, M. S. Elwan, N. R. Dessouki, *World J. Surg. Oncol.* **2007**, *5*, 4.
- [44] J. Zheng, L. Sun, W. Yuan, J. Xu, X. Yu, F. Wang, L. Sun, Y. Zeng, *Journal of oral pathology & medicine: official publication of the International Association of Oral Pathologists and the American Academy of Oral Pathology* **2018**, *47*, 830.
- [45] M. Retout, H. Valkenier, E. Triffaux, T. Doneux, K. Bartik, G. Bruylants, *ACS Sens.* **2016**, *1*, 929.
- [46] D. Aili, R. Selegard, L. Baltzer, K. Enander, B. Liedberg, *Small* **2009**, *5*, 2445.
- [47] C. C. Huang, Y. F. Huang, Z. H. Cao, W. H. Tan, H. T. Chang, *Anal. Chem.* **2005**, *77*, 5735.
- [48] H. Wei, B. L. Li, J. Li, E. K. Wang, S. J. Dong, *Chem. Commun.* **2007**, 3735.
- [49] H. Q. Liu, P. F. Rong, H. W. Jia, J. Yang, B. Dong, Q. Dong, C. J. Yang, P. Z. Hu, W. Wang, H. T. Liu, D. B. Liu, *Theranostics* **2016**, *6*, 54.
- [50] M. Grzelczak, J. Pérez-Juste, P. Mulvaney, L. M. Liz-Marzán, *Chem. Soc. Rev.* **2008**, *37*, 1783.
- [51] P. Chen, M. T. Chung, W. McHugh, R. Nidetz, Y. Li, J. Fu, T. T. Cornell, T. P. Shanley, K. Kurabayashi, *ACS Nano* **2015**, *9*, 4173.
- [52] B.-R. Oh, N.-T. Huang, W. Chen, J. H. Seo, P. Chen, T. T. Cornell, T. P. Shanley, J. Fu, K. Kurabayashi, *ACS Nano* **2014**, *8*, 2667.